Modeled Radiative Forcing Differences from Cirrus Extinction Inputs Derived from HSRL and Standard Backscatter Lidar Techniques

Scott C. Ozog

A Scholarly Paper Submitted in Partial Fulfillment of the Requirements for the Degree of Master of Science

April 2017

Department of Atmospheric and Oceanic Science
University of Maryland College Park, Maryland

Academic Advisor: Dr. Russell Dickerson
Research Advisor: Dr. Matthew McGill (NASA GSFC)
Co-Research Advisor: Dr. John Yorks (NASA GSFC)

List of Figures

List of Abbreviations

ACATS	Airborne Cloud-Aerosol Transport System
APB	Attenuated Particulate Backscatter
ARB	Attenuated Rayleigh Backscatter
ATB	Attenuated Total Backscatter
CPL	Cloud Physics Lidar
FSR	Free Spectral Range
GSFC	Goddard Space Flight Center
HOE	Holographic Optic Element
HSRL	High Spectral Resolution Lidar
ITCZ	Intertropical Convergence Zone
IR	Infrared
MC	Multichannel
LW	Longwave
NASA	National Aeronautics and Space Administration
NIR	Near Infrared
SW	Shortwave
WMO	World Meteorological Organization

List of Symbols

A_n	etalon transmission parameter
α_p	particulate extinction coefficient
α_m	molecular extinction coefficient
β_p	particulate backscatter coefficient
β_m	molecular backscatter coefficient
C	Calibration Factor
λ	wavelength
nm	nanometer
N	number of photon counts
N_{FSR}	free spectral range in units of channels
sr	steradian
S_p	particulate lidar ratio
T	Two-way transmission
$\Delta\lambda_{FSR}$	free spectral range in units of wavelength
Δd_D	etalon defect parameter
Δr	range bin width

Abstract

Cirrus are the most common cloud type in the atmosphere (Stubenrauch *et al.* 2013); having a large influence on Earth's radiative energy balance. The Airborne Cloud Aerosol Transport System (ACATS) Lidar, used to measure profiles of cirrus optical and special properties, has flown onboard the NASA ER-2 high altitude aircraft during three field campaigns since its first deployment in 2012. ACATS is a high spectral resolution lidar (HSRL), which has the ability to discriminate between the particulate and molecular components of the lidar return signal. This allows for the direct calculation of optical properties, such as particulate extinction and particulate backscatter coefficients, without assuming a lidar ratio, which is common with standard backscatter lidars analyses (Fernald et al. 1972 and Klett 1981, 1985). Proper calibration of the ACATS etalon is crucial in achieving this separation of signal (Mcgill, 1996); however, during ACATS' three field campaigns, automated in-flight calibration of the etalon was not consistently reliable due to the speed of the aircraft and the variability of the scene observed. A new calibration technique has been developed using a scattering medium within the ACATS telescope itself, and is proving to be a viable option for improving in-flight calibration of the etalon. Accurate etalon calibration leads to greater confidence in the optical properties calculated from ACATS data compared to those calculated from standard lidar data due to the absence of the lidar ratio assumption. This ultimately leads to more realistic model output, which incorporates these optical properties as input parameters. While HSRL lidars provide more accurate optical properties, they are more expensive and more difficult to implement than a standard backscatter lidar. Coincident cirrus data between the NASA ACATS HSRL and the NASA CPL standard backscatter lidar will be collected, from both ground and air platforms, to explore the differences in retrieved optical properties. I will incorporate these optical properties into the radiative transfer (RT) model, VLIDORT, on the NASA Discover super computer to quantify how altering cirrus extinction values and microphysical properties influences top of the atmosphere (TOA) radiative forcing.

1. Introduction

1.1 Importance of Cirrus

Cirrus clouds, which are composed of ice particles and found in Earth's upper troposphere, and sometimes lower stratosphere (Sassen, 1991; Murphy *et al*., 1990; Wang *et al*., 1996), play a crucial role in modulating Earth's radiative energy budget. Low and mid-level tropospheric clouds, composed of spherical liquid water droplets, are optically thicker than high cirrus clouds, and block more incoming shortwave (SW) solar radiation; cooling the underlying atmosphere. Cirrus clouds, however, are relatively transmissive to incident SW radiation while at the same time absorptive to longwave (LW) terrestrial radiation (Stephens 2005). This weak albedo effect combined with a relatively stronger greenhouse effect leads to a generalization that cirrus cause a net positive TOA radiative forcing (RF) (Liou, 1986); in other words the standard thinking is that cirrus exacerbate global warming (IPCC, 2013). Globally, cirrus are the most common cloud type, having occurrence frequencies of 40-60% (Mace *et al.* 2009). In the mid-latitudes frequencies are around 30-40%, and in the tropics they can be as high as 90% (Wang and Sassen 2002; Martins *et al.* 2011a). Cirrus clouds also impose possible positive climate feedbacks where their effective warming potentially induces further warming. Cirrus downward LW flux is directly related to the surface-cloud temperature difference. In a warmer atmosphere cirrus heights are expected to increase leading to a greater surface-cloud temperature contrast, and therefor a greater LW forcing component (Liou, 1986). Although cirrus net RF can be an order of magnitude less than lower liquid water clouds (Campbell *et al.* 2016) their occurrence frequencies make them a profound contributor to Earth's climate system. Despite their importance, large uncertainties remain with respect to cirrus formation and associated radiative properties. Making cirrus parameterization a key source of uncertainty in numerical simulations and global circulation models (GCM) (Del Genio 2002).

Cirrus microphysical properties including particle size, particle shape, number density, and ice water content (IWC) exhibit large variability dependent on the conditions under which they form (Sassen, 2001). These microphysical properties determine cirrus optical properties such as extinction, backscatter, and optical depth, which correspond to their magnitude of net RF. Taking into account the distribution of microphysical properties through the cirrus layer along with layer height and surface albedo, cirrus can display a net negative RF instead of exclusively positive (Zhang *et al*. 1990; Campbell *et al.* 2016). The temperature, humidity, and formation mechanism in which cirrus develop primarily determine these microphysical properties (Magono and Lee 1966; Pruppacher and Klett, 1997), and separates cirrus clouds into four sub categories; synoptic, injection, mountain-wave, and cold trap (Sassen, 2001). It should be noted that there is a fifth anthropogenic category, contrail cirrus, which will not be discussed. Synoptic cirrus encompass those formed under the influence of large scale synoptic flow that can elevate moist air, and promote ice crystal nucleation; such as jet stream dynamics, fronts, and Rossby Wave interactions. Injection cirrus are the mesoscale counterpart to the synoptic category, which form in relation to strong convective updrafts and anvil outflow, or blow off. Globally, injection cirrus are the most common due to the high prevalence of convective activity along the intertropical convergence zone (ITCZ) (Nazaryan *et al.*

2008). Mountain wave and cold trap cirrus are relatively less common being geographically confined to orographic regions and the tropics, respectively. Cold trap cirrus form under cold (<-70°C) high altitude (>15 km) conditions, which are found almost exclusively in the tropics.

1.2 Observations of Cirrus Properties

There are many instruments available for measuring cirrus optical and microphysical properties. Passive remote sensors such as radiometers are used to measure the emissivity of cloud layers at specific wavelengths. Liou *et al.* (1990) demonstrated a technique where the emissivity difference between two channels on the polar orbiting advanced very-high-resolution radiometer (AVHRR) were used to calculate cloud optical depth. Sassen and Comstock (2001) used a combination of ground based lidar and radiometer data, known as the LIRAD method (Platt and Dilley 1981), to develop a parameterization for cirrus optical depth based in layer thickness and mid-cloud temperature. Passive remote sensing systems are limited by their inability to provide information on the vertical structure of a layer. These platforms are also susceptible to contamination from additional emitting sources either in front of, or beyond, the intended target layer if not accurately filtered (Meyer and Platnick 2010).

In-situ probes flown on aircraft through cirrus clouds provide valuable measurements of microphysical properties, and have found significant differences between mid-latitude synoptic cirrus and tropical convective cirrus (Sassen and Benson 2001; Wang and Sassen 2002; Lawson *et al.* 2001, 2006a, 2006b; Yorks *et al.* 2011a). Lawson *et al.* (2006a) reported in mid-latitude synoptic cirrus 99% of the total number concentration of particles were <50μm. Of those crystals >50μm 50% were made up of rosette like habits, 40% were irregularly shaped, and the remaining few percent exhibited column or spheroidal habits. This is in agreement with Lawson *et al.* (2001), which found a high percentage of rosette shaped crystals in mid-latitude cirrus based on observations using the Cloud Particle Imager (CPI). Examples of ice crystal habits imaged by CPI are shown in figure 1. Conversely, column and plate habits have been more commonly observed in anvil cirrus, while rosettes less frequent. Convective cirrus exhibit a higher concentration of larger particles on the order of 100-400μm, and IWC is also higher in convective cirrus compared to synoptic (Lawson *et al.* 2006a, 2010; Noel *et al.* 2004). It has been found that ice crystal size distributions in cirrus layers are often bi-modal, including a small (<100μm) mode and a larger mode (Mitchell *et al.* 1996; and Koch 1996). In-situ probes are a key component in collecting direct measurements of cirrus microphysical properties, however these instruments also have difficulty providing vertical profiles of data and can potentially shatter crystals before measurement (Zhao *et al*. 2011).

The microphysical properties determine cirrus optical properties, and their associated radiative properties. Net RF is defined as the difference in net downward SW and net upward LW radiative flux [Wm^{-2}] (Chylek and Wong, 1998), and is estimated using numerical radiative transfer (RT) models. The influence on surface temperature through sustained TOA RF is defined as $\Delta T = \lambda * RF$, where λ represents a climate sensitivity parameter (IPCC, 2013). The sensitivity parameter can vary substantially between different forcing agents, the horizontal distribution of RF, and with latitude

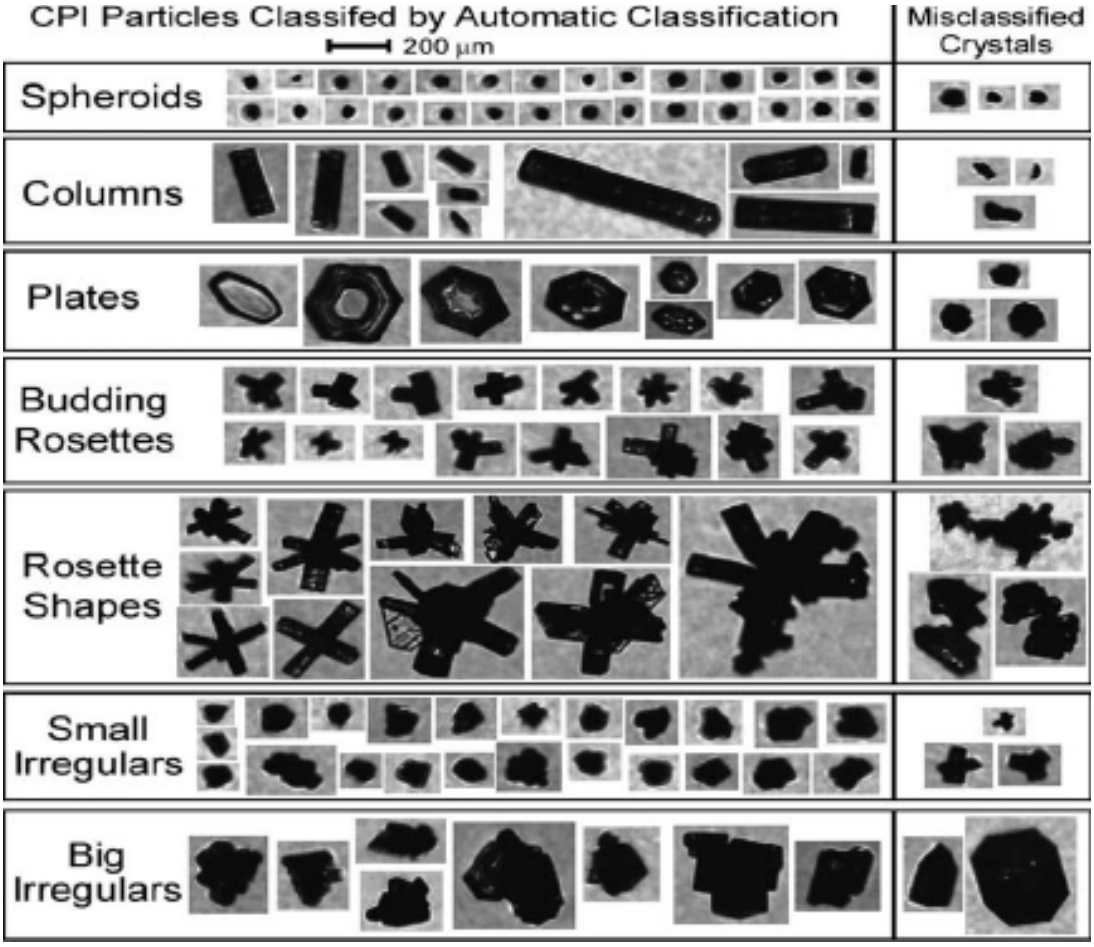

Figure 1: Cirrus ice particle habits imaged by the CPI instrument presented in Lawson *et al.* 2006a

(Forster *et al.* 2007; Shindell and Faluvegi, 2009). One of most influential optical properties is the estimated extinction, or cloud optical depth (COD), which expresses how much signal is removed from an incident beam due to absorption and scattering, and is a primary user input required to run RT simulations. Extinction values used in simulations are derived from passive or active remote sensing systems. Microphysical properties are often parameterized in these simulations based on previous in-situ studies. McFarquhar *et al*. (2000) found tropical thin cirrus have a RF as high as 5 Wm^{-2} with an average of 1.58 Wm^{-2} using lidar derived extinction values, and assumed column crystal habits. Lee *et al.* (2009) also looked at tropical thin cirrus RF, and found slightly lower values around 1.00 ± 0.07 Wm^{-2} using Moderate Resolution Imaging Spectroradiometer (MODIS) derived optical depths, and varying crystal habit distributions dependent on crystal size. Hong *et al.* (2016) calculated the zonally averaged cirrus RF over all latitude belts for a range of varying optical depths, and found forcing to be up to 15 Wm^{-2} in the tropics. The mid-latitudes exhibited a seasonal dependence with values as low as -30 Wm^{-2} in the summer, and 10 Wm^{-2} in the winter. This study used optical depths retrieved from satellite radar, *CloudSat* (Stephens *et al.* 2002), and lidar, Cloud-Aerosol Lidar and Infrared Pathfinder Satellite Observations (CALIPSO; Winker *et al.* 2003), and the

crystal shape was limited to one aggregate habit. Campbell *et al.* (2016) looked at a year of daytime mid-latitude zenith pointing lidar data, and found an estimated RF of 0.07-0.67 Wm^{-2}. This study also identified very thin cirrus (COD ≤0.01) as having a net negative RF. Zhang *et al*. (1999) performed a modeling studying on the sensitivity of cirrus RF to varying microphysical properties. This study determined that cirrus with a bi-model distribution of crystal sizes, common in cirrus clouds, wherein the second mode being of a large crystal size (>170 μm), had a net negative RF. A net negative RF was also found in cirrus with a large number density ($>10^7$ m^{-3}) of small crystals (<30 μm). Reducing uncertainty in measurements of cirrus layer microphysical and optical properties is a requirement for improving cloud parameterization in GCMs, and is an imperative area of climate change research (McFarquhar *et al.* 2000; Lee *et al.* 2009; Yorks 2014).

Currently, lidar instruments are one of the best tools available for measuring cirrus optical properties. Passive remote sensors such as MODIS are limited by their inability to obtain the vertical structure of cirrus clouds. In-situ probes like CPI flown through cirrus layers provide valuable direct measurements of microphysical properties, however, these instruments are also limited by their inability to provide full vertical profiles (Zhao *et al.* 2011). Remote sensing radar systems like *CloudSat*, which work similarly to lidar, often cannot detect thinner cirrus at the longer wavelengths in which they operate (Comstock *et al.* 2002).

1.3 Cirrus Profile Retrievals and Lidar Techniques

The primary method for collecting vertical profiles of cirrus spatial and optical properties is through the use of a lidar instrument. There are several different variations of lidar with the two most common used for measuring cloud-aerosol profiles being a standard backscatter lidar and an HSRL. Both of these lidars measure the elastic backscatter of emitted laser light from atmospheric molecules and particulates. Lidars are important because their data provides full atmospheric profiles of spatial and optical properties where there is no fully attenuating layer. This data is provided at both temporal and spatial resolutions that cannot be met by in-situ instruments, passive remote sensors, or similar radar remote sensors alone.

Standard backscatter lidars are currently the most common lidar used for retrieving profiles of clouds and aerosols. These types of lidar are the least complex to implement, relatively inexpensive, and have been providing reliable ground and air based measurements for decades. For example, the NASA Cloud Physics Lidar (CPL) is a standard backscatter lidar that flies on the NASA ER-2 high altitude aircraft, and has flown on over two dozen field campaigns since its first deployment in 2000. CPL operates at 355nm, 532nm, and 1064nm wavelengths, and produces optical properties for its visible and near infrared (NIR) channels (*McGill et al.* 2002). Standard backscatter and HSRL lidars initially derive atmospheric profiles of attenuated total backscatter (ATB) from their raw photon counts. The ATB is composed of a molecular (Rayleigh) component and a particulate (Mie) component; however, it yields no knowledge of either of these components alone. ATB can be written as a function of the backscatter (β) and extinction (α) coefficient optical properties, which also both contain a molecular (β_m, α_m) and particulate component (β_p, α_p) (*Eq. 1.1)*. N(r) are the number of photons per range

$$ATB = \frac{N(r)r^2}{C} = \beta(r)T^2(r,\alpha) \begin{cases} \beta(r) = \beta_A(r) + \beta_M(r) \\ T^2(r) = \exp\{-2\int[\alpha_A(r) + \alpha_M(r)]dr \end{cases} \quad \text{Eq. 1.1}$$

bin, T^2 is the two-way transmission, and C is a calibration factor composed of instrument parameters. The molecular components of both coefficients can be computed from profiles of temperature and humidity provided by either a model or a World Meteorological Organization (WMO) upper air radiosonde. Once this is done the two particulate components are the only unknowns remaining, but with only one equation. To calculate the particulate components a lidar ratio first must be assumed to reduce the number of unknowns down to one (Fernald *et al.* 1972; Klett 1981). This is the primary challenge faced calculating optical properties from standard backscatter lidar data. The lidar ratio used is assumed to be homogeneous throughout a given particulate layer, whether it's a cirrus cloud, water cloud, or an aerosol layer. Lidar ratios can vary from 10 to 100 steradians (sr) depending on the type of cloud or aerosol. The error in this assumed lidar ratio propagates through to the calculation of the optical properties, and then further into the output from a radiative transfer model that incorporates the optical properties as input. An error in the assumed lidar ratio of just 5 sr can cause approximately a 20% error in the retrieval of the extinction coefficient (Young *et al*. 2013).

The benefit of an HSRL is that a lidar ratio does not have to be assumed when calculating optical properties. HSRL lidars contain an additional filter within their receiver sub-system for differentiating the signal between its molecular and particulate components. This will be referred to as the HSRL technique, and it is made possible by taking advantage of the difference in spectral broadening that light undergoes when scattered by air molecules as compared to atmospheric particulates. At visible wavelengths air molecules will broaden the signal approximately 10^{-3} nm (Young 1981), and particulates broaden the signal two orders of magnitude less approximately 10^{-5} nm (Esselborn *et al.* 2008). Figure 2 depicts an idealized transmission peak from photons scattered by an atmospheric particulate. The blue curve represents the wide broadening caused by the air molecules, while the red curve represents the narrow broadening caused by the particulates. This greater broadening from the air molecules is caused by their high velocities, which are a result of their random thermal motions. Unlike standard backscatter lidars, which utilize only one channel at each wavelength they operate (unless they have depolarization capabilities), HSRLs will use more than one channel for a given wavelength, those for retrieving the molecular signal and those for the particulate signal. The NASA ACATS HSRL uses an etalon (Fabry Perot Interferometer) as its filter to separate the lidar signal into its two components. An etalon consists of two parallel optically flat plates with reflective dielectric coatings on their respective sides facing one another. Light that enters the etalon is transmitted through the first plate into the space between the two of them. Here the light undergoes multiple reflections between each plate where light is either reflected or transmitted. Most light is reflected back out of the etalon with a small percentage transmitted through to the imaging plane. The amount of light an etalon transmits is a function of the reflectivity of the plates, and the etalon plate

loss. Light transmitted through the etalon undergoes constructive and destructive interference, appearing as a fringe pattern (Figure 3) on the imaging plane. Each white ring represents light that has undergone constructive interference, and has a wavelength different from the next concentric ring. This difference in wavelength is referred to as the free spectral range (FSR). The FSR is a function of the original wavelength entering the etalon, plate spacing, and the index of refraction between the plates. The transmitting laser must be highly stable to stay aligned with the etalon filter, and must maintain this stability in the environment of the ER-2 aircraft, making ACATS more difficult and expensive to implement.

ACATS has a 24 channel detector array used to retrieve the signal from the innermost ring of the fringe, and utilizes a holographic optical element (HOE), called the circle to point converter, that focuses the full circular pattern of the ring onto each detector so the entirety of the signal is captured instead of just a small arc. While there are several methods of making an HSRL lidar, utilizing an etalon to image the fringe pattern on to an array of detectors is referred as the multichannel (MC) method (McGill and Spinhirne 1998). The MC method allows ACATS to directly measure both components of the signal without any assumptions, which HSRL lidars using an iodine filter must do (Piironen and Eloranta, 1994). The grey shaded region in figure 2 represents the detection region that ACATS measures. The molecular signal appears as a flat background signal across all the channels, and the sharp peak represents the particulate signal. Integrating this flat line of the ACATS spectrum across all channels yields the molecular component, and then subtracting that from the total signal and integrating across the remaining peak will yield the particulate component. Simply integrating the entire signal across all channels, and then calibrating the signal similarly to how you would with a standard backscatter lidar would produce the same ATB product. However, the HSRL can produce the attenuated Rayleigh backscatter (ARB) and the attenuated particulate backscatter (APB), which make up the ATB. I use weighted least-squares linear fitting method developed by McGill (1996) to retrieve the ARB and APB from the raw photon counts.

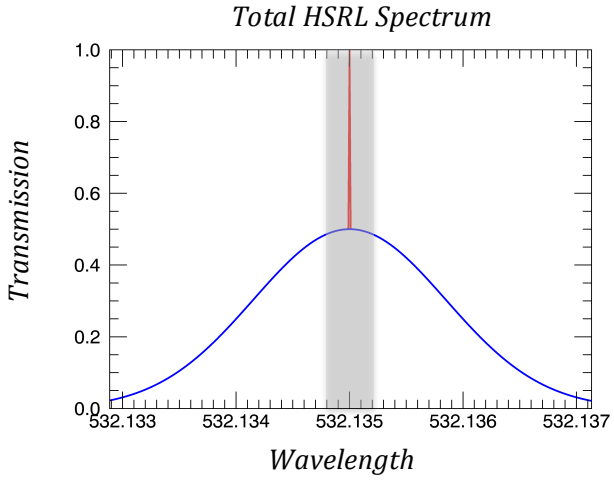

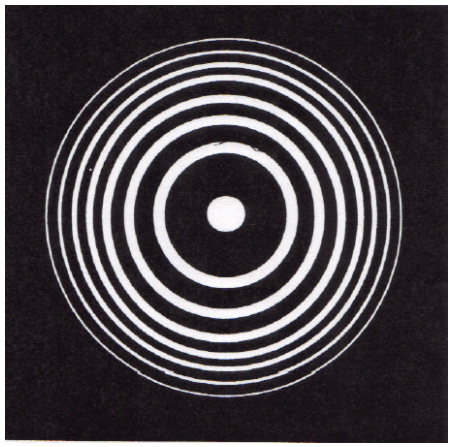

Figure 2 (left): Transmission spectrum of the Rayleigh (blue) and particulate (red) broadening for atmospheric backscattered light at 532nm. **Figure 3 (right):** Etalon fringe pattern caused by the destructive and constructive interference of the light between the two reflective plates

2. Preliminary Research

2.1 Etalon Calibration

For the least-squares fitting routine to accurately retrieve the ARB and APB, defects within the etalon first must be accounted for. Ideally the two plates of the etalon would have no loss of signal and would be perfectly parallel. However, microscopic defects on the plates can cause issues of non-parallelism, which decrease the transmission of the etalon and broaden the transmitted spectrum as well. This is seen across the ACATS channels as the peak caused by particulate backscatter being broader and spread across more channels than if there were no defects. An etalon calibration procedure for an MC HSRL lidar was developed by McGill *et al.* (1997a) and operationally implemented on ACATS during its field campaigns by Yorks (2014). Software onboard ACATS runs a calibration procedure, referred to as an etalon scan, which uses piezoelectric actuators to adjust the gap between the etalon plates. The spacing between the plates on the ACATS etalon is set to 10cm when no etalon scan is taking place, and the gap is adjusted on the order of picometers during the scan. Adjusting the spacing between the etalon plates acts to move the fringe pattern across the 24 channels of the detector array. During an etalon scan two orders of each channel's response are measured, meaning the peak will move across each channel twice before a scan is completed. An etalon calibration value, defect parameter, can then be determined for each channel by using a least squares fitting technique of the etalon transmission function

$$T(\Delta\lambda, j) = \sum_{n=0}^{\infty} A_n \cos\left[2\pi n\left(\frac{\Delta\lambda}{\Delta\lambda_{FSR}} + \frac{j}{N_{FSR}}\right)\right] \sin c\left(\frac{n}{N_{FSR}}\right) \qquad \text{Eq. 2.1}$$

$$A_n = 2\left(1 - \frac{1}{1-R}\right)^2 \left(\frac{1-R}{1+R}\right) R^n e^{-4\pi n^2 \Delta_D^2 \lambda_o^2} \qquad \text{Eq. 2.2}$$

Table 2.1. Etalon transmission function variables

Variable	Description
A_n	etalon transmission parameter
j	ACATS channel number
n	number of iterations
R	etalon plate reflectivity
$\Delta\lambda_{FSR}$	etalon free spectral range
$\Delta\lambda$	wavelength offset of initial wavelength and scan wavelength

(*Eq. 2.1*) to the measured response from each channel during the etalon scan. Equation 2.2 expands the etalon transmission parameter (A_n) from the etalon transmission function, and the defect parameter (Δd_D^2) is highlighted yellow. Table 2.1 provides a definition of variables in the transmission function. The correct defect parameter is determined through an iterative process of changing its value in the transmission function to determine which value yields the best fit to each channel. The process starts at a value of

zero and is increased by intervals of 1.0 to a maximum of 100. The value that yields the best reduced chi squared value when fit is determined to be the defect value for that channel.

2.2 Improved Etalon Calibration

Since 2012 the ACATS instrument has flown in three field campaigns during which etalon scans had been performed mid-flight. Etalon scans performed with zenith pointing lab data cannot be used on aircraft data because the environmental conditions at which the etalon operates are different. The temperature and pressure inside the instrument are different in the lab than compared to flying on board the ER-2 at an altitude of 20km. Thus, etalon scans must be performed during in flight under the conditions that the etalon has been operating, and used to collect data. During these field campaigns defect values retrieved from etalon calibration scans were not consistently reliable due to the non-uniformity of the signal from varying backscatter targets and the speed of the aircraft (200 ms^{-1}). Figures 4a and b show calibration fits from etalon scans performed during ACATS' last field campaign in August of 2015. The measured channel response is shown in red, and the fitted transmission function is shown in blue. Figure 4a is an example of the response in channel 1 from an etalon scan performed during a flight on August 19th, 2015. This response appears to have a good periodic structure and a broad fit transmission function. However, this example yielded defect values that were too high. Figure 4b shows the response in channel 13 from a flight the next day, and is an example of how poor the spectral response can be from in-flight calibration. To have the most accurate etalon scan possible the signal must be invariant. It was originally designed that the stratospheric Rayleigh signal just below the aircraft would be used for

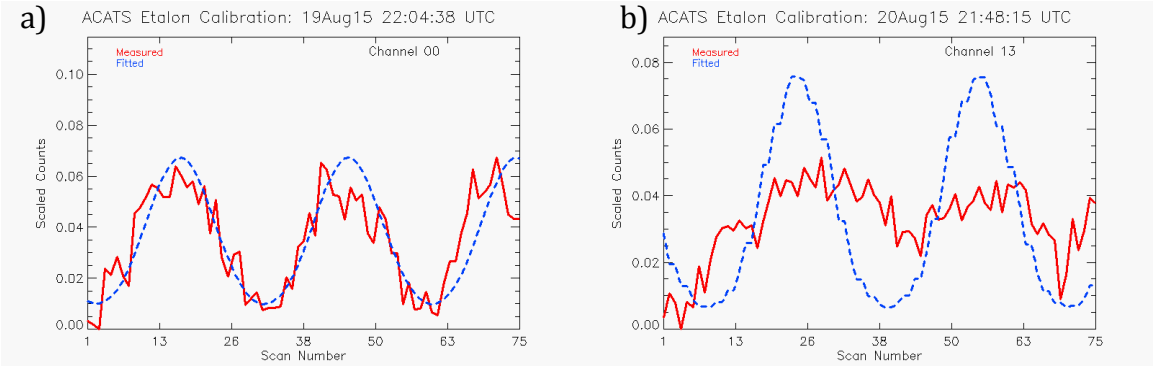

Figure 4a. The calibration fit for ACATS channel 1 from an etalon scan performed on August 19th, 2015 with red representing the spectral response, and blue the transmission function. (**b)** The calibration fit for channel 13 from a scan performed during a flight the next day on August 20th.

calibration, but the molecular signal at this altitude was too weak for viable calibration.

A new calibration technique has been successfully tested, and will soon be operationally implemented, for improving the reliability of etalon scans that are performed mid-flight. Instead of using the signal backscattered by the atmosphere, it was theorized, and proven, that a scattering medium inside the ACATS telescope itself placed

in the path of the laser could be used during calibration instead. This eliminates the aforementioned issue of a variable scene at high speeds resulting in inconsistent etalon scans. Etalon scans performed for zenith pointing ground data are also improved; as they are susceptible to the same errors from a varying scene. A material that produces the peak spectral response expected, and also withstands high intensity laser light on the order of 30 minutes without experiencing any deformation was necessary. It was determined that white Delrin plastic placed in the path of the laser achieved the desired results. However, using the delrin alone saturated the detectors so it was also discovered that neutral density filters along with a light dispersing element needed to be placed over the fiber optic tip leading back into the optics box. Figure 5 shows the spectral response in channel 1 from an etalon scan performed in the lab using this configuration. The observed sharp peak and near perfect fit of the transmission function is what's expected

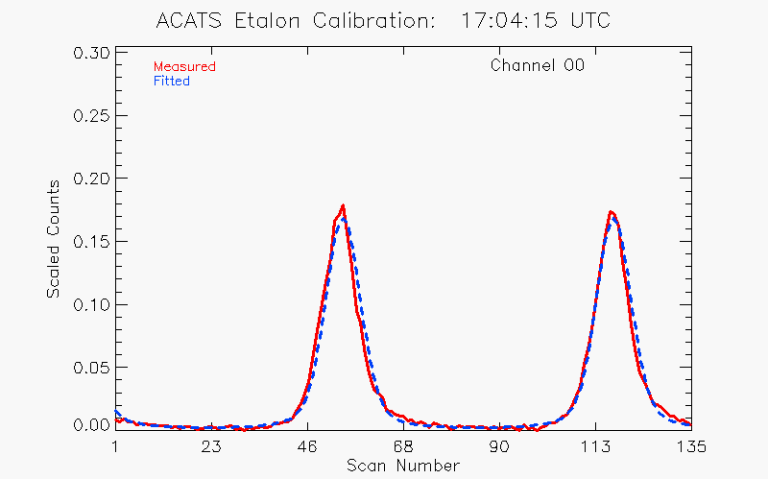

Figure 5. Spectral response in ACATS channel 1 from a etalon scan performed in the lab using the new method of white delrin plastic inside the telescope as a scattering medium

in accurate etalon calibration.

Once the optimal configuration was determined, testing began to ensure that this method was repeatable. To gain knowledge of the reliability of etalon scans from the previous method, the etalon scans from the seven most recent field campaign flights were compared to one another. Figure 6b is a plot showing the average defect values across all the channels from those flights, as well as their standard deviation and coefficient of variation. The defect values recovered from the science flights are inconsistent and exhibit variability as high as almost 50% in some channels. For comparison seven etalon scans using the new method were run over the coarse of seven different days. Only one scan was done a day to mimic the conditions ACATS would operate in the field, in which the instrument is fully shutdown after a science flight, and then turned on and warmed back up on the next day. Figure 6a shows the same statistics as 6b, but for the seven consecutive lab tests performed. Unlike the defect values from the in-flight etalon scans, the lab tests yielded consistent values consistent with low variability of around 10%. Modeling studies were done to estimate the improvement made to ACATS extinction retrievals with the new calibration values. As shown in figure 6, the defect variation for inflight calibration was between 20-50 for most channels, and between 0-10 for lab calibration. A simulated atmospheric scene was constructed from radiosonde data, and

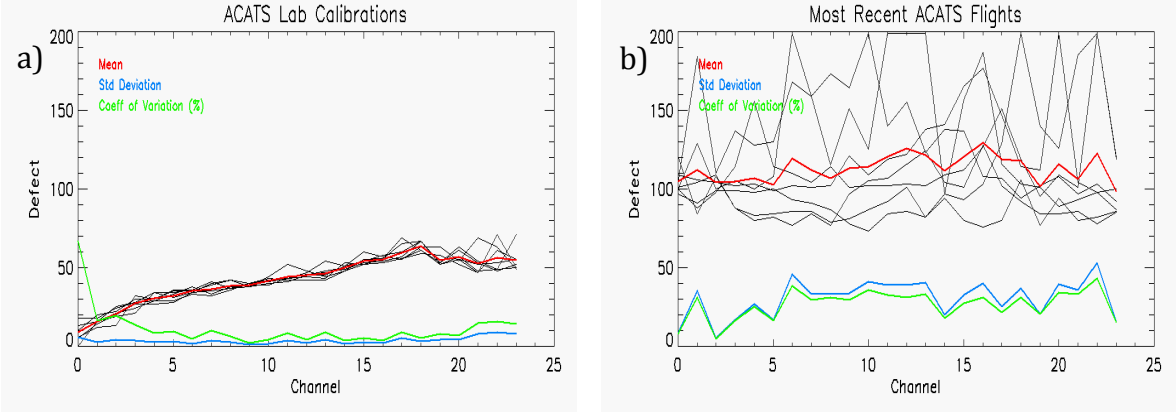

Figure 6. Mean, standard deviation, and coefficient of variation defect values from consecutive etalon scans performed in the lab using the new delrin scattering method **(a)** and comparison statistics from the seven most recent etalon scans performed during flights from the last two field campaigns **(b)**.

an embedded cirrus layer between 9 and 11km with a constant extinction of 0.2 km^{-1}. The ACATS photon counts were simulated at the instruments native 60m range bins, and the average to 360m for calculating the optical properties. The absolute error in defect values was increased from 0 to 30 in intervals of 5. Extinction values with a defct error of 30 had errors on the order of 100%. Extinction values with defect errors of 0-10 had considerably less error around 0-20%.

2.3 Lab Retrievals and Results

The mean defect values from the lab tests were used to retrieve the ARB and APB from zenith pointing data taken in the lab at NASA Goddard Space Flight Center (GSFC) of a thick cirrus layer that passed over on March 10th, 2016. The least squares linear fitting method developed by McGill (1996) was successfully used to separate the lidar signal into its respective components on this day. Figures 7a-d depict what a successful separation of the signal looks like compared to an unsuccessful separation. This step is crucial in moving forward with the accurate retrieval of optical properties from ACATS data. Figures 7a-b show the ARB and APB, respectively, from the zenith pointing data of the cirrus layer taken on March 10th, 2016. Figures 7c-d show the ARB and APB, respectively, of thin cirrus clouds and aerosol data taken on August 19th, 2015 over southern California during ACATS last field campaign. The cirrus layer over GSFC is seen between 7 and 9 km through the entire image in figure 7b. There are also two small cirrus layers in the first half of the image at around 11 km. The APB image for March 10th also has no Rayleigh signal below the cirrus layer, indicated by the black coloring. Comparing the APB image to the ARB image from March 10th the cirrus layer has been completely removed, and the Rayleigh signal is now visible; indicated by the purple coloring that has appeared below 7km. Figures 7c-d conversely do not show a proper separation of the particulate and Rayleigh signal. The APB image for the August 19th does have some of the Rayleigh signal removed, however some of it is still visible in the first half of the image. The second half of the image has spotty cirrus clouds visible

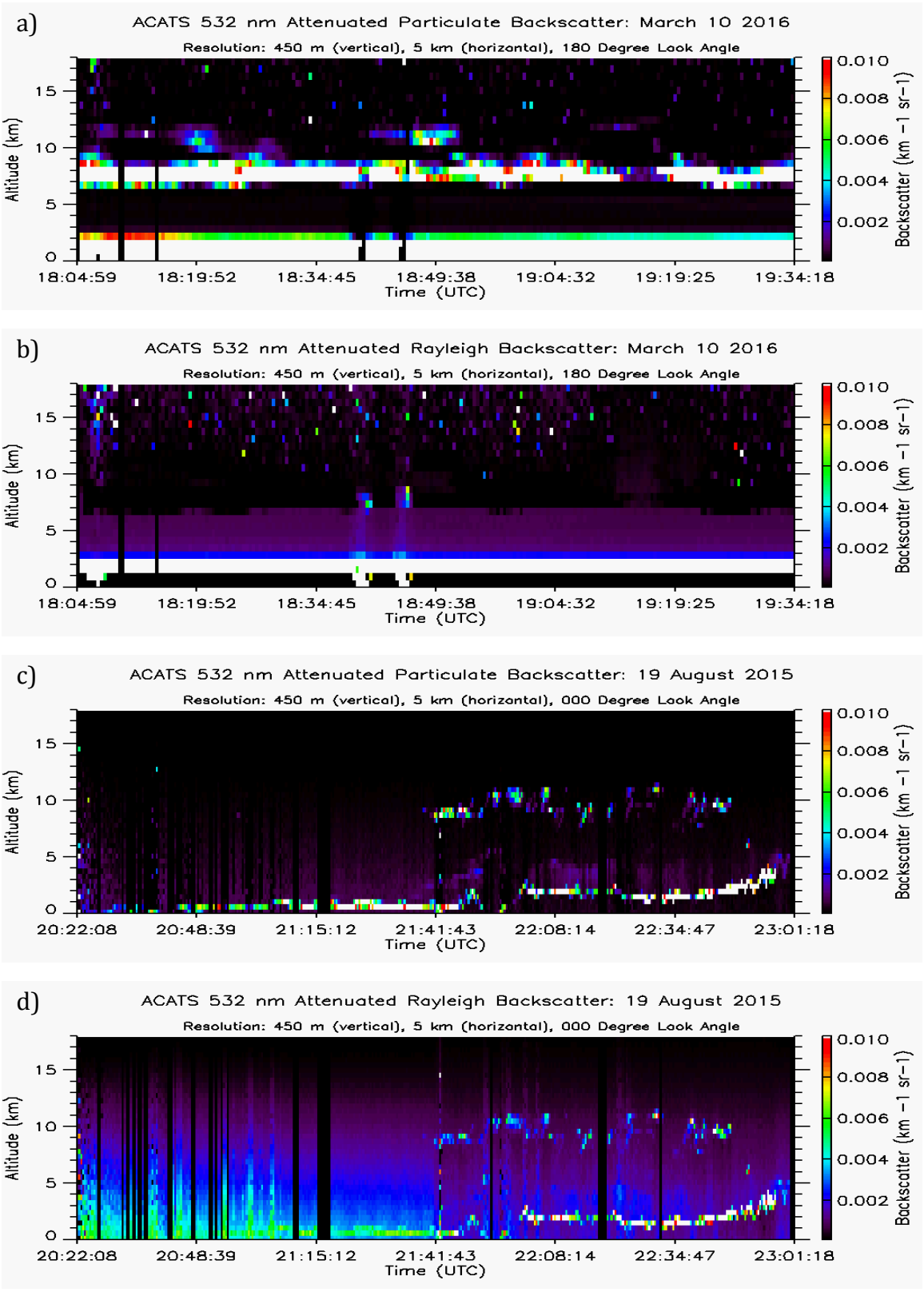

Figure 7. The APB **(a)** and ARB **(b)** of a cirrus layer observed from the lab at NASA GSFC on March 10th, 2016 compared to the APB **(c)** and ARB **(d)** of scattered thin cirrus and aerosols observed during a science flight on August 19th, 2015 over Southern California.

between 9 and 11 km, and weakly scattering aerosol layers indicated by the purple coloring near the ground. The Rayleigh signal in the ARB image is much stronger compared to the APB image, as expected, however little to none of the particulate signal has been removed with the cirrus clouds and aerosols still visible. Since the APB and ARB from March 10th were accurately retrieved they were then be used to directly calculat the optical properties for the cirrus layer observed. Figure 8 shows the extinction coefficients calculated for the March 10th scene. Since these extinction coefficients are directly calculated without any assumptions, they have less uncertainty than those that would be calculated using the Klett method of assuming a constant lidar ratio for the cirrus layer. Lidar ratios for cirrus clouds can range from 20-40 sr (Seifert *et al*. 2007, Yorks *et al.* 2011a) depending on their microphysical properties. Yorks (2014) showed that ACATS derived extinction values from the WAVE campaign at Wallops Island had uncertainties of 15-20%. Comparatively, those derived from the CPL standard backscatter lidar had uncertainties greater than 50%.

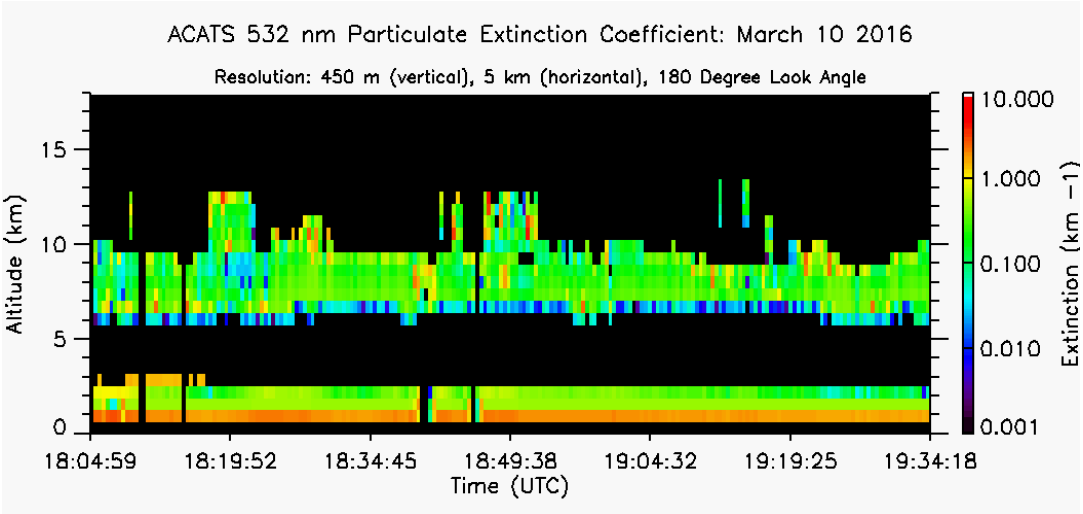

Figure 9. Extinction values calculated for the cirrus layer observed on March 10th, 2016 over NASA GSFC.

3. Proposed Research

Today only a handful of HSRL lidars are in operation nationwide, in which only a few operate on an airborne platform. When ACATS and CPL fly together in their next deployment it will be the first time an MC HSRL will provide consistently reliable etalon calibration from an airborne platform. It is clear that the original method of calibrating the etalon mid-flight during field campaigns produced inconsistent results, and is not a viable option for accurate HSRL retrievals. Moving forward, I will assist our engineering team in modifying the ACATS receiver subsystem to integrate the Delrin scattering medium and neutral density filters. After which, operators will be able to manually send a command to the ACATS instrument during data collection to enter it into an etalon scan. This will engage servo motors, placing the filters and Delrin into position; putting ACATS in proper etalon calibration configuration. ACATS will fly on-board the ER-2 with its new configuration in summer or fall 2017, and will collect simultaneous data

with the NASA CPL standard backscatter lidar during its next deployment. Until then I will collect concurrent zenith pointing data from the lab at NASA GSFC. This side-by-side operation of the two instruments will provide a nearly direct comparison between the HSRL directly calculated and the standard backscatter derived optical properties along with their associated radiative effects. The overall scientific goal is to improve characterization of mid-latitude cirrus radiative effects, and elucidate how contrasting instrument techniques can affect lidar data. This study consists of three main objectives:

1. **Quantify improvements made to ACATS HSRL optical properties and determine contrast with Klett method retrievals for cirrus subtypes.**

Signal separation is crucial in computing HSRL optical properties, which have less uncertainty than those calculated from the Klett method. The Klett method assumes the lidar ratio to be constant through an entire particulate layer, which introduces potential error as lidar ratios can significantly vary both horizontally and vertically. Yorks (2014) demonstrated that extinction uncertainty in HSRL retrievals were up to 50% lower than for standard backscatter retrievals. Young *et al.* (2013) showed an error in the assumed lidar ratio of just 5 sr can cause approximately 20% error in the retrieved extinction coefficient. Defect values retrieved from the improved calibration technique will enable the direct retrieval of molecular and particulate signal components, and is applicable to both airborne and zenith pointing ground operations. MC HSRL lidars offer an advantage to other HSRL techniques because they directly retrieve the aerosol and molecular signals simultaneously. The current standard in HSRL retrievals is to use an iodine filter to separate the signal into its total and molecular components, and infer the particulate signal from the difference between the total and molecular signal. This subjects the aerosol signal to potential molecular contamination if the molecular signal is not properly calibrated. There have been many lidar studies dedicated to studying cirrus optical properties (Sassen and Comstock 2001; Martins *et al.* 2011; Yorks *et al.* 2011a). However, these studies were conducted using standard backscatter lidar, and there remain large uncertainties in the differences between coincident HSRL and standard backscatter lidar retrievals. This is due to the fact that HSRL lidars are more expensive and difficult to implement because they require a highly stable laser that must stay aligned with the optical filter (Yorks, 2014). Emphasis in this study will be placed on contrasting the retrieved optical properties for a large cirrus dataset between the HSRL and Klett method. I will specifically be comparing ACATS and CPL lidar ratios, and the calculated particulate extinction coefficients.

ACATS and CPL operating side-by-side will provide the first known robust comparison between an HSRL and standard backscatter lidar. Previously, ACATS data sets were limited to its three field campaigns, which were further limited to few reliable HSRL optical profiles from accurate etalon calibration. Using the two lidars I will build a comprehensive dataset of cirrus subtypes consisting of winter and summertime synoptically generated cirrus, and summertime convective cirrus. Ten hours of data for each respective subtype will be collected, which will result in over 1400 well calibrated profiles of each. This time will be parsed into at least ten different collection days to create a dataset not overly represented by any single scene or cirrus event. The months between October and April will define the wintertime synoptic cirrus, and the months of

May through September will define the summertime synoptic along with the period convective cirrus is expected to potentially form. As mentioned in section 1.1, synoptic cirrus will be associated with formation under large scale dynamics such as frontal systems, Rossby waves, and jet streams. Convective cirrus will be considered anvil blow from nearby convective activity determined using satellite and radar imagery. The NOAA GOES-13 geostationary satellite provides near real time imagery of the eastern CONUS with a 30-minute temporal resolution, and yields a comprehensive view of clouds associated with evolving patterns. For ground based zenith operations the ACATS HSRL products are calculated at a resolution of 25 seconds horizontally and 360m vertically. CPL provides optical properties at a finer resolution of one second horizontal, and 30m vertically (Hlavka *et al* 2012). However, in order to retain continuity between the two instruments the CPL products will be averaged to 25 seconds horizontally and 360m vertically, to match the ACATS resolution.

2. Determine potential biases in the assumed lidar ratios used by standard backscatter lidars.

Currently, there are many standard backscatter lidars that have been operating over long periods of time, and contain expansive datasets. The Cloud-Aerosol Lidar with Orthogonal Polarization (CALIOP) aboard the Cloud-Aerosol Lidar and Infrared Pathfinder Satellite Observation (CALIPSO) satellite (Winker *et al.* 2009) has been providing cloud and aerosol profiles in its sun-synchronous orbit since launched in 2006. The Cloud-Aerosol Transport System (CATS) onboard the International Space Station (ISS) has been operational since March 2015, and has already emitted more laser pulses than CALIPSO. The Micro Pulse Lidar Network, operated by NASA, consists of multiple stationary zenith pointing lidars operating at varying locations across the globe (Welton *et al.* 2001). As mentioned in section 1.3, the CPL standard backscatter lidar has participated in over two dozen field campaigns since its first deployment in 2000.

Comparing ACATS' directly retrieved lidar ratios to CPL's assumed lidar ratio over a variety of cirrus subtypes provides a unique opportunity to improve standard backscatter lidar data. The lidar ratio must first be assumed before calculating the extinction and COD from standard backscatter data. Decreasing the uncertainty in the assumed lidar ratio would result in a decreased uncertainty in these calculated optical properties. Biases found in comparing the coincident ACATS and CPL lidar ratios will lead to an understanding of how these two techniques vary, and lead to improvements in standard backscatter retrieved optical properties. As standard backscatter lidars are much cheaper and easy to implement, their use is unlikely to dwindle in place of HSRLs, which makes the improvement of standard backscatter retrieved optical properties a significant task. Using a global distribution of CALIPO lidar ratios from 2006-2010, Yorks (2014) showed cirrus lidar ratios are more influenced by their dynamic formation mechanism rather than the respective aerosol loading of different geographic regions acting as ice nuclei (IN). I will produce the same results for the entire current CATS dataset for comparison with the CALIPO version, and then recreate them using biases found between the compared ACATS and CPL data.

In addition to coincident ACATS and CPL data, comparison scenes will also be collected from a CALIPO overpass, and another from a CATS overpass. Due to the

conditional and spatial dependence of a comparison between the ground and space based systems, only one comparison scene will be retrieved for each satellite for a winter and summertime synoptic scenario. There will not be a planned attempt to capture convective cirrus with a satellite overpass due to the relatively small temporal and spatial scales of convective activity (~100km). Synoptic spatial scales are on the order of 1000km. Therefore, an overpass will be deemed acceptable for comparison with the GSFC based lidars if it is determined the cirrus captured at both locations developed under the same synoptic conditions through the use of upper level charts and satellite imagery. Along with the GOES-13 satellite, the MODIS imagers onboard the Aqua and Terra sun-synchronous A-Train satellites provide higher resolution images than GOES-13 during their early afternoon overpasses (a common time data collection takes place).

3. Refine RF estimates for mid-latitude cirrus subtypes, and quantify net cirrus TOA radiative forcing differences between contrasting extinction inputs.

Globally, cirrus are the most common cloud species with occurrence frequencies around 40-60% (Mace *et al.* 2009). Despite their relatively weak RF, compared to lower liquid water clouds (Campbell *et al.* 2016), their prevalence and variability make them one of the most influential components to Earth's radiative energy balance. However, the representation of cirrus in GCMs still remains a large source of uncertainty (IPCC, 2007). As discussed in section 1.2, cirrus TOA RF estimates can vary depending on the instrument used for optical property retrievals, geographic location, and the parameterization of microphysical properties (McFarquhar 2000; Lee *et al.* 2009; Hong *et al.* 2016). RF simulations using lidar derived optical properties have the advantage of full layer profiles, where the signal is not fully attenuated, and optically thinner layers that radar remote sensing systems cannot detect. However, previous cirrus RF studies incorporating lidar data often use standard backscatter lidars, assuming a lidar ratio for extinction profile calculations. Atmospheric extinction is a crucial component in modulating Earth's radiation budget, and is also a primary user input incorporated into radiative transfer models.

Utilizing ACATS and CPL together I will calculate TOA radiative forcing using a powerful RT model, refining current mid-latitude cirrus estimates through more accurate cirrus representation. The Vector Linearized Discrete Ordinate Radiative Transfer (VLIDORT) model (Spurr, 2006) run on the NASA Discover super computer at the NASA Center for Climate Simulation (NCCS) will be used for simulating cirrus profiles and estimating their RF. VLIDORT is written in Fortran, and is already compiled on Discover. Simulations are executed through a Python script that specifies the input parameters, and then calls the RT code. VLIDORT uses the discrete ordinate method (Chandrasekhar, 1950) for developing radiative transfer solutions in a plane-parallel pseudo-spherical (PS) atmosphere, and allows for a large amount of customization by the user to simulate the desired profile. Required inputs include total optical thickness of the layer (lidar optical properties), single scattering albedo, and the scattering phase matrix of the ice crystals. Additionally, the number of layers desired and their respective temperature and pressure can be specified to represent a refractive atmosphere. Atmospheric temperature and pressure will be provided by the same radiosonde launch used in initial processing of the lidar data. The scattering phase matrices used during

simulations will be those developed by Dr. Ping Yang's research group at Texas A&M, which have developed an expansive database of ice particle optical properties (Yang *et al.* 2013). This extensive work includes scattering properties for nine different crystal habits, three types of surface roughness, and a large range of crystal sizes (2.0-10^4 μm). The microphysical parameterizations, such as ice crystal size distribution, habit, and phase function will be determined based on complimentary cirrus studies (Lawson *et al.* 2001; 2006a; 2010). Heymsfield *et al.* (2014) showed cloud IWC can be estimated based on layer temperature and the volume extinction coefficient. CPL's additional infrared channel with depolarization capabilities provides information regarding particle shape and size. More irregularly shaped ice crystals, like columns, with large aspect ratios (ratio of length to width) have higher depolarization ratios around 0.5. Crystals with smaller aspect ratios, like spheroids, have lower depolarization ratios around 0.2 (Noel *et al.* 2004; Sassen and Benson 2001). CPL also provides profiles of backscatter color ratio (ratio of 1064nm to 532nm backscatter), which yields information on crystal size. Color ratios can range from 0.50 to 1.4 for cirrus clouds, and are directly correlated with particle size (Del Guasta and Niranjan, 2001). Coincident CPL and ACATS data provides an excellent opportunity to better tune the model to the observed cirrus properties with HSRL optical retrievals, and microphysical information from CPL. As mentioned above, at least ten separate scenes for each cirrus type will be collected, each of which I will model with varying microphysical parameterizations dependent upon the cirrus type, CPL depolarization ratios, and CPL color ratios. Comparison simulations will also be run where I alter cirrus layer extinctions between ACATS and CPL derived values, which will elucidate how different instrument methods can affect radiative forcings. These results will also be applicable to future lidar instrument proposals, such as the NASA Aerosol-Cloud-Ecosystem (ACE), as to which lidar type will be more suitable for the associated science goals.

References

Baran, A. J., On the scattering and absorption properties of cirrus cloud, J. Quant. Spectrosc. Radiat. Transfer 89, 17-36 (2004).

Bucholtz, A., D. L. Hlavka, M. McGill, K. S. Schmidt, P. Pilewskie, S. M. Davis, E. A. Reid, and A. L. Walker, 2010: Directly measured heating rates of a tropical subvisible cirrus cloud, *J. Geophys. Res*., **115**, D00J09, doi:10.1029/2009JD013128.

Campbell, J., S. Lolli, J. Lewis, Y. Gu, and E. Welton, 2016: Daytime Cirrus Cloud Top-of-the-Atmosphere Radiative Forcing Properties at a Midlatitude Site and Their Global Consequences. *J. Appl. Meteor. Climatol.,* **55**, 1667–1679, doi: 10.1175/JAMC-D-15-0217.1.

Chandrasekhar, S. 1950: Raditive Transfer, Oxford Univ. Press, Oxford.

Chylek, P. and Wong, J. G. D.: Cloud radiative forcing ratio – An analytical model, Tellus A, 50, 259–264, 1998.

Comstock, J. M., T. P. Ackerman, and G. G. Mace, 2002: Groundbased lidar and radar remote sensing of tropical cirrus clouds at Nauru Island: Cloud statistic and radiative impacts. *J. Geophys. Res*., **107**, 4714, doi:10.1029/2002JD002203.Up

Del Genio, A. D., 2002: GCM simulations of cirrus for climate studies. Cirrus, D. K. Lynch et al., Eds., Oxford University Press, 310–326.

Del Guasta, M., and K. Niranjan, 2001: Observation of Low-Depolarization Contrails at Florence (Italy) using a 532–1064 nm Polarization LIDAR, Geophys. Res. Lett., 28(21), 4067–4070

Esselborn, M., M. Wirth, A. Fix, M. Tesche, and G. Ehret, 2008: Airborne high spectral resolution lidar for measuring aerosol extinction and backscatter coefficients. *Appl. Opt*, **47**, 346– 358.

Fernald, F.G., B. M. Herman and J. A. Reagan, 1972: "Determination of aerosol height distributions with lidar", *Journal of Applied Meteorology*, **11**, 482-489.

Forster, P., et al., 2007: Changes in Atmospheric Constituents and in Radiative Forcing. In: Climate Change 2007: The Physical Science Basis. Contribution of Working Group I to the Fourth Assessment Report of the Intergovernmental Panel on Climate Change [Solomon, S., D. Qin, M. Manning, Z. Chen, M. Marquis, K. B. Averyt, M. Tignor and H. L. Miller (eds.)] Cambridge University Press, Cambridge, United Kingdom and New York, NY, USA, 129-234.

Heymsfield, A., D. Winker, M. Avery, M. Vaughan, G. Diskin, M. Deng, V. Mitev, and R. Matthey, 2014: Relationships between ice water content and volume extinction coefficient from in situ observations for temperatures from 08 to 2868C: Implications for spaceborne lidar retrievals. J. Appl. Meteor. Climatol., 53, 479–505, doi:10.1175/JAMC-D-13-087.1.

Hlavka, D. L., J. E. Yorks, S. A. Young, M. A. Vaughan, R. E. Kuehn, M. J. McGill, and S. D. Rodier, 2012: Airborne validation of cirrus cloud properties derived from CALIPSO lidar measurements: Optical properties. J. Geophys. Res., 117, D09207, doi:10.1029/2011JD017053.

Hong, Y., G. Liu, and J.-L. F. Li, 2016: Assessing the radiative effects of global ice clouds based on CloudSat and CALIPSO measurements. J. Climate, 29, 7651–7674, doi:10.1175/ JCLI-D-15-0799.1.

Intergovernmental Panel on Climate Change (2007), Climate Change 2007: IPCC Fourth Assessment Report, Cambridge Univ. Press, Cambridge, U. K.

IPCC, 2013: Climate Change 2013: The Physical Science Basis. Contribution of Working Group I to the Fifth Assessment Report of the Intergovernmental Panel on Climate Change [Stocker, T.F., D. Qin, G.-K. Plattner, M. Tignor, S.K. Allen, J. Boschung, A. Nauels, Y. Xia, V. Bex and P.M. Midgley (eds.)]. Cambridge University Press, Cambridge, United Kingdom and New York, NY, USA, 1535 pp, doi:10.1017/CBO9781107415324.

Klett, J. D., 1981: Stable analytical inversion solution for processing lidar returns. *Appl. Opt*, **20**, 211–220.

Klett, J. D., 1985: Lidar inversion with variable backscatter/extinction ratios. *Appl. Opt*, **24**, 1638–1643.

Koch, W., 1996. Solarer Strahlungstransport in Arktischem Cirrus. PhD Thesis. GKSS 96/E/60, 99 pp.

Lawson, R. P., B. A. Baker, C. G. Schmitt, and T. L. Jensen, 2001: An overview of microphysical properties of Arctic clouds observed in May and July 1998 during FIRE ACE, J. Geophys. Res., 106, 14,989–15,014, doi:10.1029/2000JD900789.

Lawson, R. P., B. A. Baker, B. Pilson, and Q. Mo, 2006a: In Situ observations of the microphysical properties of wave, cirrus and anvil clouds. Part II: Cirrus clouds, J. Atmos. Sci., 63, 3186–3203, doi:10.1175/JAS3803.1.

Lawson, R. P., E. Jensen, D. L. Mitchell, B. Baker, Q. Mo, and B. Pilson, 2010: Microphysical and radiative properties of tropical clouds investigated in TC4 and NAMMA, J. Geophys. Res., 115, D00J08, doi:10.1029/2009JD013017.

Lee, J., P. Yang, A. E. Dessler, B. C. Gao, and S. Platnick, 2009: Distribution and radiative forcing of tropical thin cirrus clouds. J. Atmos. Sci., 66, 3721–3731, doi:10.1175/2009JAS3183.1.

Liou, K.-N.: Influence of cirrus clouds on weather and climate processes: A global perspective, Mon. Weather Rev., 114, 1167– 1199, 1986.

K. N. Liou, S. C. Ou, Y. Takano, F. P. J. Valero, and T. P. Ackerman, "Remote sounding of the tropical cirrus cloud temperature and optical depth using 6.5 and 10.5 pim radiometers during STEP," J. Appl. Meteorol. 29, 716-726 (1990)

Mace, G. G., Q. Zhang, M. Vaughan, R. Marchand, G. Stephens, C. Trepte, and D. Winker, 2009:Adescription of hydrometeor layer occurrence statistics derived from the first year of merged CloudSat and CALIPSO data. J. Geophys. Res., 114, D00A26, doi:10.1029/2007JD009755.

Magono, C., and C. W. Lee, 1966: Meteorological classification of natural snow crystals. J. Fac. Sci., Hokkaido Univ., Ser. 7, 2, 321–335.

Martins, E., V. Noel, and H. Chepfer, 2011: Properties of cirrus and subvisible cirrus from nighttime Cloud-Aerosol Lidar with Orthogonal Polarization (CALIOP), related to atmospheric dynamics and water vapor, J. Geophys. Res., 116, D02208, doi:10.1029/2010JD014519.

McFarquhar, G. M., and Coauthors, 2000: Thin and subvisual tropopause tropical cirrus: Observations and radiative impacts, *J. Atmos. Sci*., **57(12)**, 1841– 1853, doi:10.1175/1520-0469(2000)057<1841:TASTTC>2.0.CO;2.

McGill, M.J., 1996: Recovery and Validation of Wind and Aerosol Profiles from Incoherent Doppler Lidar Measurements. PhD Thesis, University of Michigan (Ann Arbor, MI).

McGill, M. J., W. R. Skinner, and T. D. Irgang, 1997a: Analysis techniques for the recovery of winds and backscatter coefficients from a multiple channel incoherent

McGill, M.J., and J.D. Spinhirne, 1998: Comparison of two direct-detection Doppler lidar techniques, *Opt. Eng*., **37**, 2675–2686.

McGill, M. J., D. Hlavka, W. Hart, V. S. Scott, J. Spinhirne, and B. Schmid, 2002: Cloud Physics Lidar: instrument description and initial measurement results. *Applied Optics*, **41**, 3725-3734.

Meyer, K. G., and S. Platnick, 2010: Utilizing the MODIS 1.38 μm channel for cirrus cloud optical thickness retrievals: Algorithm and retrieval uncertainties, *J. Geophys. Res.*, **115**, D24209, doi:10.1029/2010JD014872.

D.L. Mitchell, S.K. Chai, Y. Liu, A.J. Heymsfield, Y. Dong, 1996: Modeling cirrus clouds. Part I: Treatment of bimodal size spectra and case study analysis. J. Atmos. Sci., 53 (1996), pp. 2952–2966

Murphy, D. M., Kelly, K. K., Tuck, A. F., Proffitt, M. H., and Kinne, S.: Ice saturation at the tropopause observed from the ER-2 aircraft, Geophys. Res. Lett., 17, 353–356, 1990.

Noel, V., D. M. Winker, M. McGill, and P. Lawson, 2004: Classification of particle shapes from lidar depolarization ratio in convective ice clouds compared to in situ observations during CRYSTAL-FACE, J. Geophys. Res., 109, D24213, doi:10.1029/2004JD004883.

Piironen P. and E.W. Eloranta, 1994: Demonstration of a high-spectral-resolution lidar based on an iodine absorption filter. Opt. Lett., 19, 234–236.

Platt, and A. C. Dilley, 1981: Remote sounding of high clouds. Part IV: Observed temperature variations in cirrus optical properties. J. Atmos. Sci., 38, 1069–1082.

Pruppacher, H. R., and J. D. Klett, 1997: Microphysics of Clouds and Precipitation. Kluwer Academic, 954 pp.

Sassen, K. 1991: Corona-producing cirrus cloud properties derived from polarization lidar and photographic analyses, Appl. Opt., 30, 3421–3552.

Sassen, K., 2001: Cirrus: A Modern Perspective. Cirrus, D. Lynch et al., Eds., Oxford University Press, in press.

Sassen, K., and S. Benson, 2001: A midlatitude cirrus cloud climatology from the Facility or Atmospheric Remote Sensing. Part II: Microphysical properties derived from lidar depolarization. J. Atmos. Sci., 58, 2103– 2112.

Sassen, K., and J. M. Comstock, 2001: A midlatitude cirrus cloud climatology from the Facility for Atmospheric Remote Sensing. Part III: Radiative properties. J. Atmos. Sci., 58, 2113–2127.

Seifert, P., Ansmann, A., Müller, D., Wandinger, U., Althausen, D., Heymsfield, A. J.,Massie, S. T., and Schmitt, C., 2007: Cirrus optical properties observed with lidar,radiosonde, and satellite over the tropical Indian ocean during the aerosol-pollutednortheast and clean maritime southwest monsoon, J. Geophys. Res., 112, D17205, doi:10.1029/2006JD008352.

Shindell, D., and G. Faluvegi, 2009: Climate response to regional radiative forcing during the twentieth century. Nature Geosci., 2, 294–300.

Spurr RJD. VLIDORT, 2006: A linearized pseudo-spherical vector discrete ordinate radiative transfer code for forward model and retrieval studies in multilayer multiple scattering media. J Quant Spectrosc Radiat Transfer, 102, 316–42

Stephens, G. L., 2005: Cloud feedbacks in the climate system: A critical review, *J. Climate*, **18**, 237-273

Stubenrauch, C. J., and Coauthors, 2013: Assessment of global cloud datasets from satellites. Bull. Amer. Meteor. Soc., 94,

Wang, P. H., Minnis, P., McCormick, M. P., Kent, G. S., and Skeens, K. M.: A 6 year climatology of cloud occurrence frequency from stratospheric aerosol and gas experiment II observations (1985– 1990), J. Geophys. Res., 101, 29407–29429, 1996.

Wang, Z., and K. Sassen, 2002: Cirrus cloud microphysical property retrieval using lidar and radar measurements. Part I: Algorithm description and comparison with in situ data. J. Appl. Meteor., 41, 218–229.

Welton, E. J., J. R. Campbell, J. D. Spinhirne, and V. S. Scott, 2001: Global monitoring of clouds and aerosols using a network of micro-pulse lidar systems. Lidar Remote Sensing for Industry and Environmental Monitoring, U. N. Singh, T. Itabe, and N. Sugimoto, Eds., International Society for Optical Engineering (SPIE Proceedings, Vol. 4153), 151–158.

Winker, D. M., M. A. Vaughan, A. H. Omar, Y. Hu, K. A. Powell, Z. Liu, W. H. Hunt, and S. A. Young, 2009: Overview of the CALIPSO Mission and CALIOP Data Processing Algorithms. J. Atmos. Oceanic Technol., 26, 1105-1119, doi:10.1175/2009JTECHA1281.1.

Yang, P., L. Bi, B.A. Baum, K.-N. Liou, G.W. Kattawar, M.I. Mishchenko, and B. Cole, 2013: Spectrally consistent scattering, absorption, and polarization properties of atmospheric ice crystals at wavelengths from 0.2 μm to 100μm, J. Atmos. Sci., 70, 330-347.

Young, A.T., 1981: Rayleigh scattering. *Phys. Today*, **35**, 42–48.

Yorks, J. E., D. L. Hlavka, W. D. Hart, M. J. McGill, 2011a: Statistics of Cloud OpticalProperties from Airborne Lidar Measurements. J. Atmos. Oceanic Technol., 28, 869–883. doi: http://dx.doi.org/10.1175/2011JTECHA1507.1

Yorks, J.E., 2014: An Investigation of Cirrus Cloud Properties Using Airborne Lidar. PhD Thesis, University of Maryland (College Park, MD)

Zhang, Y., A. Macke, and F. Albers, Effect of crystal size spectrum and crystal shape on stratiform cirrus radiative forcing, Atmos. Res. 52, 59-75 (1999).

Zhao, Y., G. G. Mace, and J. M. Comstock, 2011: The occurrence of particle size distribution bimodality in midlatitude cirrus as inferred from ground-based remote sensing data, *J. Atmos. Sci.*, **68**, 1162–1177, doi:10.1175/2010JAS3354.1.